

## Reconstruction of High Contrast 2-D Conductivities by the Algorithm of A. Nachman

Samuli Siltanen, Jennifer L. Mueller, and David Isaacson

ABSTRACT. The uniqueness proof of A. Nachman [20] for the 2D inverse conductivity problem outlines a reconstruction algorithm for determining the unknown conductivity in a region  $\Omega$  from knowledge of the Dirichlet-to-Neumann map. The algorithm is a direct method based on the techniques of inverse scattering. Here we present a practical implementation of the algorithm in Nachman's proof and demonstrate its effectiveness on several radially symmetric conductivities in  $C^3(\Omega)$  and  $C^4(\Omega)$ .

### 1. Introduction

Let  $\Omega \subset \mathbb{R}^2$  be a bounded, simply connected  $C^\infty$  domain and  $\gamma \in C^2(\Omega)$ . We assume that  $\gamma(x) \geq c > 0$  and  $\gamma \equiv 1$  in a neighborhood of  $\partial\Omega$ .

Define the Dirichlet-to-Neumann map corresponding to  $\gamma$  by

$$(1.1) \quad \Lambda_\gamma : H^{1/2}(\partial\Omega) \rightarrow H^{-1/2}(\partial\Omega), \quad \langle \Lambda_\gamma f, g \rangle = \int_\Omega \gamma \nabla u \cdot \nabla v,$$

where  $v$  is any  $H^1(\Omega)$  function with trace  $g$  on the boundary and  $u$  is the unique  $H^1(\Omega)$  solution of the Dirichlet problem

$$(1.2) \quad \begin{cases} \nabla \cdot \gamma \nabla u &= 0 \text{ in } \Omega, \\ u &= f \text{ on } \partial\Omega. \end{cases}$$

The inverse conductivity problem of Calderón [7] is to decide whether  $\gamma$  is uniquely determined by  $\Lambda_\gamma$  and if so, reconstruct  $\gamma$  from the knowledge of  $\Lambda_\gamma$ . Physically,  $u$  represents the electric potential and  $\gamma$  the conductivity. Knowledge of the Dirichlet-to-Neumann map is tantamount to knowing the resulting current pattern on  $\partial\Omega$  corresponding to any prescribed voltage pattern on  $\partial\Omega$ . The inverse problem has applications in geophysics, nondestructive testing and a medical imaging technique known as Electrical Impedance Tomography (EIT). In EIT the domain  $\Omega$  is often a cross-section of the body, such as a patient's chest. A basis of current patterns is applied on electrodes attached around the patient's chest and the resulting voltages are measured on the electrodes. Since the tissues and organs in the body have

---

2000 *Mathematics Subject Classification.* 35R30.

The second author was supported by an NSF Mathematical Sciences Postdoctoral Fellowship.

## 2. The reconstruction algorithm

In this section we give a brief outline of the reconstruction algorithm set forth in Nachman's uniqueness proof [20].

First, the conductivity equation (1.2) is transformed to the Schrödinger equation by the following change of variables. Let  $q \in C_0^0(\Omega)$  be given by

$$q = \gamma^{-1/2} \Delta \gamma^{1/2}.$$

If  $u$  is a solution of  $\nabla \cdot \gamma \nabla u = 0$  in  $\Omega$ , defining  $\tilde{u} = \gamma^{1/2} u$  yields

$$(2.1) \quad (-\Delta + q)\tilde{u} = 0 \text{ in } \Omega.$$

While in [20] the first step is to find  $\gamma|_{\partial\Omega}$  and  $\partial\gamma/\partial\nu|_{\partial\Omega}$  and to continue  $\gamma$  artificially to be one outside a neighborhood of  $\Omega$ , we omit that step in this work and consider only conductivities that are one in a neighborhood of  $\partial\Omega$ . This assumption allows us to smoothly extend  $\gamma = 1$  and  $q = 0$  to the whole plane. We may therefore study equation (2.1) in all of  $\mathbb{R}^2$ .

The exponentially behaving solutions of (2.1) introduced by Faddeev [11] are the key to the reconstruction. By Theorem 1.1 of [20] for any  $k \in \mathbb{C} \setminus 0$  there is a unique solution  $\psi(x, k)$  of

$$(2.2) \quad (-\Delta + q)\psi(x, k) = 0 \quad x \in \mathbb{R}^2$$

satisfying  $e^{-ikx}\psi(\cdot, k) - 1 \in W^{1, \tilde{p}}(\mathbb{R}^2)$  for any  $2 < \tilde{p} < \infty$ . The space  $W^{1, \tilde{p}}(\mathbb{R}^2)$  is a special case of the definition

$$W^{m, \rho}(E) = \{f \in L^\rho(E) \mid \partial^\alpha f \in L^\rho(E), |\alpha| \leq m\}$$

for an arbitrary domain  $E \subset \mathbb{R}^n$  and  $1 \leq \rho \leq \infty, m \geq 0$ .

Denote

$$(2.3) \quad \mu(x, k) := e^{-ikx}\psi(x, k), \quad x \in \mathbb{R}^2, k \in \mathbb{C} \setminus 0.$$

Here  $ikx = i(k_1 + ik_2)(x_1 + ix_2)$ . Then  $\mu$  satisfies

$$(2.4) \quad (-\Delta - 2ik\bar{\partial} + q)\mu = 0$$

where  $\bar{\partial} = (\partial/\partial x_1 + i\partial/\partial x_2)/2$ . The condition  $\mu - 1 \in W^{1, \tilde{p}}$  and the Sobolev imbedding theorem yield that  $\mu$  is continuous and tends to one asymptotically when  $|x| \rightarrow \infty$ .

The reconstruction of  $\gamma$  is based on the use of an intermediate object called the *non-physical scattering transform*  $\mathbf{t}$ , which is not directly measurable in experiments:

$$(2.5) \quad \mathbf{t}(k) := \int_{\mathbb{R}^2} e_k(x)\mu(x, k)q(x)dx, \quad k \in \mathbb{C} \setminus 0,$$

where  $e_k(x) := \exp(i(kx + \bar{k}\bar{x}))$ . Note that since  $\mu$  is asymptotically close to one,  $\mathbf{t}(k)$  is approximately the Fourier transform of  $q(x)$  evaluated at the point  $(-2k_1, 2k_2) \in \mathbb{R}^2$ .

The direct reconstruction method consists of two main steps:

1. Given  $\Lambda_\gamma$ , determine the scattering transform  $\mathbf{t}(k)$ .
2. Determine  $\gamma$  from the knowledge of  $\mathbf{t}(k)$ .

To obtain  $\mathbf{t}(k)$  from the Dirichlet-to-Neumann data, one must first solve an integral equation for the trace on  $\partial\Omega$  of the exponentially growing solution  $\psi$ . Denote the Dirichlet-to-Neumann map of the homogeneous conductivity 1 by  $\Lambda_1$  and note that since  $\gamma \equiv 1$  near  $\partial\Omega$  the maps  $\Lambda_\gamma$  and the Dirichlet-to-Neumann

**3. From  $\Lambda_\gamma$  to  $\mathbf{t}(k)$**

In this section we describe how we obtain the scattering transform from the Dirichlet-to-Neumann map numerically. In [18] it is shown that the step from  $\Lambda_\gamma$  to  $\mathbf{t}(k)$  has only a logarithmic stability estimate while the step from  $\mathbf{t}(k)$  to  $\gamma$  has linear stability.

In [21] it is shown that if  $\gamma(x)$  is rotationally symmetric, so is  $\mathbf{t}(k)$ . In this work we consider radial conductivity distributions and make use of this fact in our construction of the Dirichlet-to-Neumann data and in our approximation of  $\mathbf{t}(k)$ . In the numerical solution of the  $\bar{\partial}$  equation, no radial symmetry of  $\gamma$  or  $\mathbf{t}(k)$  is assumed. If  $\gamma(x) = \gamma(|x|)$  we know from [23] that the functions  $\phi_n(\theta) := (2\pi)^{-1/2}e^{in\theta}$ ,  $n \in \mathbb{Z}$ , are eigenfunctions for  $\Lambda_\gamma$ . Thus  $\Lambda_\gamma$  can be represented in the trigonometric basis by the collection  $\{\lambda_n\}_{n=-\infty}^\infty$  of its eigenvalues.

To produce numerical data, we need to approximate these eigenvalues numerically. As explained in [12], we note that if two radial  $L^\infty$  conductivities  $\gamma$  and  $\tilde{\gamma}$  satisfy  $\gamma(x) \leq \tilde{\gamma}(x)$  pointwise in  $\Omega$ , the eigenvalues satisfy  $\lambda_n \leq \tilde{\lambda}_n$ . Moreover, for piecewise constant radial conductivities we can compute the eigenvalues explicitly [21]. Thus approximating the  $C^2$  conductivity from above and below with piecewise constant conductivities gives us numerical upper and lower bounds for the eigenvalues. See [21] for more details.

To obtain  $\mathbf{t}(k)$  from  $\{\lambda_n\}$  numerically, we use the approximation  $\psi(x, k)|_{\partial\Omega} \approx e^{ikx}$ , as opposed to solving the integral equation (2.6). Expanding  $e^{ikx}$  in a Fourier series on the circle  $x = e^{i\theta}$  yields [14]

$$e^{ikx} = \sum_{n=-\infty}^\infty a_n(k)e^{in\theta} \quad \text{with} \quad a_n(k) = \begin{cases} \frac{(ik)^n}{n!}, & n \geq 0 \\ 0, & n < 0. \end{cases}$$

Substituting this series into formula (2.10) gives

$$(3.1) \quad \mathbf{t}(k) \approx \mathbf{t}^{\text{exp}}(k) = \sum_{n=1}^N (\lambda_n - |n|) \frac{(-1)^n |k|^{2n}}{(n!)^2}.$$

Although one would expect this approximation to be more accurate for small  $q$ , we obtained reasonable results in our examples even when  $q$  was not small.

**4. From  $\mathbf{t}(k)$  to  $\gamma$**

By [18] the  $\bar{\partial}$  inversion  $\mathbf{t} \rightarrow \gamma$  is well-posed and even contributes some smoothing. The fact that the  $\bar{\partial}$  equation must be solved independently for each  $x$  in the region of interest to obtain  $\gamma(x)$  suggests the use of parallelization in a numerical method. Here a 2-D adaptation of the method of product integrals presented in [1] in 1-D is used to solve the  $\bar{\partial}$  equation in parallel for the  $x$  values in the region of interest. The idea of the method is to factor the integrand into its smooth part and its singular part and approximate the smooth part with a simple function, such as an interpolatory polynomial. The new integrand is then computed analytically where possible. We describe the method applied to the weakly singular second-order Fredholm integral equation (2.12) below. We mention that in the numerical solution of the  $\bar{\partial}$  equation, no radial symmetry of  $\gamma$  or  $\mathbf{t}(k)$  is assumed.

For  $s \in \mathbb{C} \setminus \{0\}$  write equation (2.12) as

$$(4.1) \quad \mu(x, s) = 1 + \frac{1}{4\pi^2} \int_{\mathbb{R}^2} H(s, k) L(x, k) \overline{\mu(x, k)} dk_1 dk_2$$

Denote  $\mu_{ji}(x) := \mu(x, (u_j, v_i))$ . By regrouping terms, the numerical integration operator in (4.5) can now be written as

$$(4.7) \quad \kappa_N \mu(x, s) = \sum_{j=1}^{N-1} \sum_{i=1}^{N-1} A^{ji}(x) \overline{\mu_{ji}(x)}$$

where

$$(4.8) \quad A^{ji}(x) = a_{ji}(x) J_{00}^{ji}(s) + b_{ji}(x) J_{10}^{ji}(s) + c_{ji}(x) J_{01}^{ji}(s) + d_{ji}(x) J_{11}^{ji}(s).$$

Choose  $\{s = (u_k, v_l)\}_{k,l=1}^N$  defining an  $N^2$  by  $N^2$  matrix  $\mathbf{A}(x) = (A^{ji}(x))$  where  $A^{ji}(x)$  is the linear combination of the  $J_{\alpha\beta}^{ji}((u_k, v_l))$  above,  $\alpha, \beta \in \{0, 1\}$ . This results in the linear system

$$(4.9) \quad \mathbf{I}\mu(x) - \mathbf{A}\bar{\mu}(x) = \mathbf{g}(x)$$

where  $\mathbf{I}$  is the  $N^2$  by  $N^2$  identity matrix. This system can be solved by equating the real and imaginary parts to obtain two linear systems in real variables with two vectors of unknowns. Namely,

$$(4.10) \quad (\mathbf{I} - \operatorname{Re}(\mathbf{A}))\mathbf{a} - \operatorname{Im}(\mathbf{A})\mathbf{b} = \operatorname{Re}(\mathbf{g})$$

$$(4.11) \quad (\mathbf{I} + \operatorname{Re}(\mathbf{A}))\mathbf{b} - \operatorname{Im}(\mathbf{A})\mathbf{a} = \operatorname{Im}(\mathbf{g})$$

where  $\mu = \mathbf{a} + i\mathbf{b}$ . Solving the linear system gives  $\{\mu(x, (u_j, v_i))\}_{j,i=1}^N$ .

Note that the factors  $J_{\alpha}^{ji}(s)$  in the matrix  $\mathbf{A}$  are independent of  $x$ , so they need only be computed once and stored. Then in parallel, the matrix  $\mathbf{A}$  is assembled by forming the linear combination (4.8) and the resulting systems (4.9) are solved.

## 5. Numerical Examples

In this section we test the algorithm on three high-contrast conductivities in  $C^3(\Omega)$  and a high contrast conductivity in  $C^4(\Omega)$  which contains a dip near the boundary of  $\Omega$ . The first three examples increase in magnitude from 4 to approximately 6 and 8. We compare the corresponding scattering transforms and the reconstructions. The conductivities for Examples 1, 2, and 3 are defined by the following formula. Fix  $0 < \rho < 1$  and let  $F_{\rho} \in C_0^3(\mathbb{R})$  be given by

$$(5.1) \quad F_{\rho}(x) := (x^2 - \rho^2)^4, \quad -\rho \leq x \leq \rho$$

and  $F_{\rho}(x) \equiv 0$  for  $|x| > \rho$ . Let

$$(5.2) \quad \gamma(x) := (\alpha F_{\rho}(|x|) + 1)^2,$$

Then the support of  $\gamma(x) - 1$  is the interval  $[-\rho, \rho]$ .

*Example 1:*  $\rho = 1/4$  and  $\alpha = 16\rho^{-6}$ .

*Example 2:*  $\rho = 1/4$  and  $\alpha = 23\rho^{-6}$ .

*Example 3:*  $\rho = 1/4$  and  $\alpha = 29\rho^{-6}$ .

The plots of  $\gamma_1$ ,  $\gamma_2$ , and  $\gamma_3$  are found with the reconstructions in Figure 2. In each of these examples, 49 eigenvalues were computed using the method described in Section 3. The upper and lower bounds were in very close agreement. The approximate scattering transform  $\mathbf{t}^{\text{exp}}(k)$  was then computed using the series (3.1) with  $N = 49$  and the lower bounds for the eigenvalues. The scattering transforms  $\mathbf{t}^{\text{exp}}(k)$  corresponding to  $\gamma_1$ ,  $\gamma_2$ , and  $\gamma_3$  are plotted in Figure 1. One observes that the scattering transform increases in amplitude with  $\gamma$ , and the divergence of the series (3.1) becomes more marked as the amplitude of  $\gamma$  increases. Reconstructions

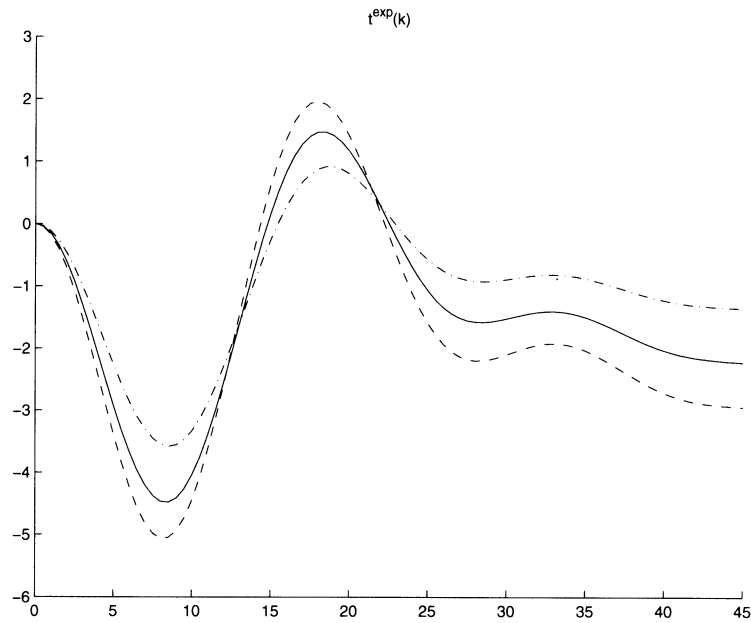


FIGURE 1. The functions  $t^{exp}(k)$  for  $\gamma_1(x)$  (dot-dashed line),  $\gamma_2(x)$  (solid line), and  $\gamma_3(x)$  (dashed line).

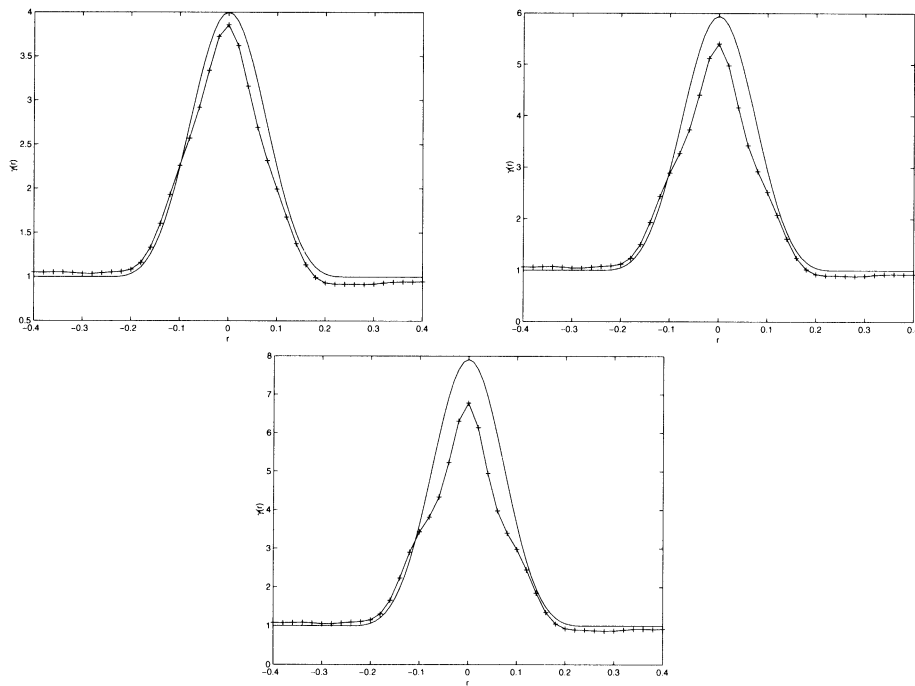


FIGURE 2. Cross-sectional plots of the reconstructed  $\gamma_i$  (-+) and the actual  $\gamma$  (-) for  $i = 1$  (upper left),  $i = 2$  (upper right), and  $i = 3$  (bottom center).

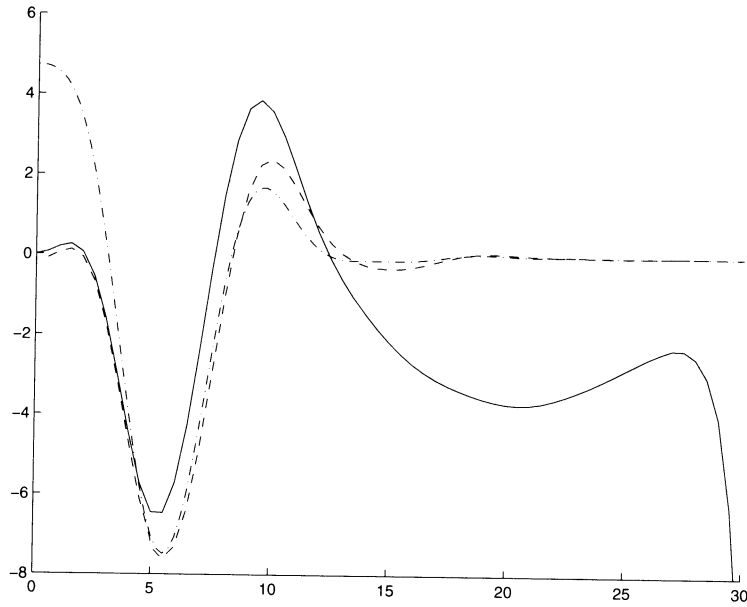


FIGURE 4. The functions  $\mathbf{t}^{exp}(k)$  (solid line),  $\mathbf{t}^{LS}(k)$  (dashed line), and  $\hat{q}(2|k|)$  (dot-dashed line) for Example 4.

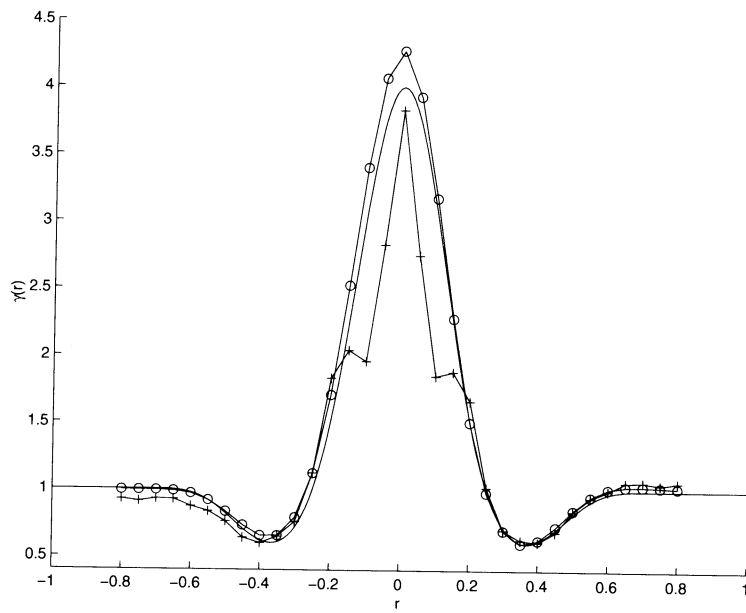


FIGURE 5. Cross-sectional plot of the reconstructed  $\gamma$  from  $\mathbf{t}^{exp}$  (-+), the reconstructed  $\gamma$  from  $\mathbf{t}^{LS}$  (-o), and the actual  $\gamma$  (solid line) for Example 4.

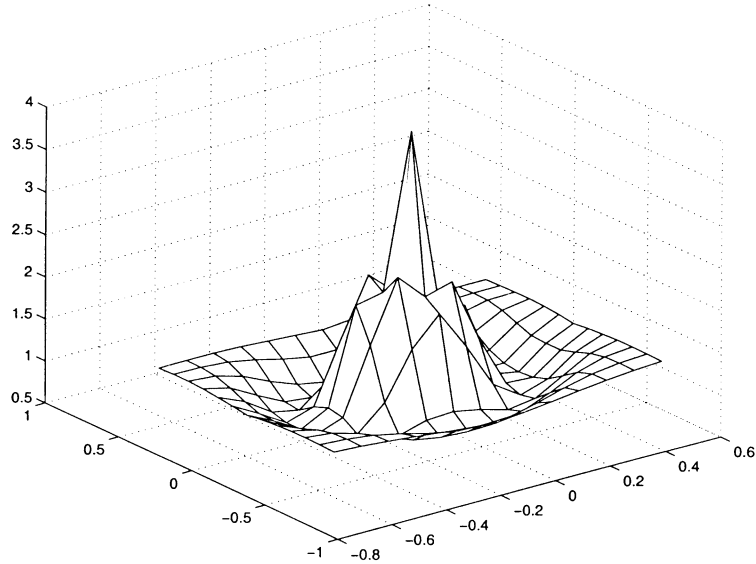


FIGURE 6. Plot of the reconstructed  $\gamma$  from  $t^{exp}$  for Example 4.

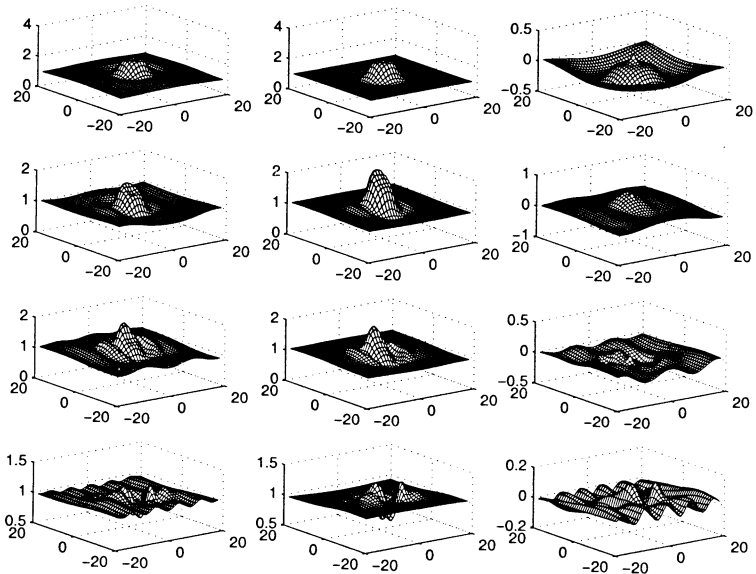


FIGURE 7. The reconstructed  $\mathfrak{R}(\mu_{exp}(x, k))$  (left column),  $\mathfrak{R}(\mu_{LS}(x, k))$  (center column) and  $\mathfrak{R}(\mu_{LS}(x, k)) - \mathfrak{R}(\mu_{exp}(x, k))$  (right column) for  $x = 0, .1, .2, .4$  (top to bottom).